Progress In Electromagnetics Research, Vol. 122, 197–221, 2012

EXTRACTION OF INTERNAL SPATIAL FEATURES OF INHOMOGENEOUS DIELECTRIC OBJECTS USING NEAR-FIELD REFLECTION DATA

D. Kurrant* **and E. Fear**

Department of Electrical and Computer Engineering, Schulich School Engineering, University of Calgary, Calgary, Alberta, T2N 1N4, Canada

Abstract—Ultra-wideband (UWB) microwave radar imaging techniques provide a non-invasive means to extract information related to an object's internal structure. For these applications, a short-duration electromagnetic wave is transmitted into an object of interest and the backscattered fields that arise due to dielectric contrasts at interfaces are measured. In this paper, we present a method that may be used to estimate the time-of-arrival (TOA) parameter associated with each reflection that arises due to a dielectric property discontinuity (or dielectric interface). A second method uses this information to identify the locations of points on these interfaces. When data are collected at a number of sensor locations surrounding the object, the collection of points may be used to estimate the shape of contours that segregate and enclose dissimilar regions within the object. The algorithm is tested with data generated when a cylindrical wave is applied to a number of numerical 2D models of increasing complexity. Moreover, the algorithm's feasibility is evaluated using data generated from breast models constructed from magnetic resonance (MR) breast scans. Results show that this is a promising approach to identifying regions and the internal structure within the breast.

1. INTRODUCTION

Exploration of alternative methods for breast imaging has included several methods based on electromagnetic properties of the tissues [1]. At microwave frequencies, breast imaging relies on differences in dielectric properties of various tissues within the breast [2]. Recent

Received 21 September 2011, Accepted 7 November 2011, Scheduled 17 November 2011

* Corresponding author: Douglas J. Kurrant (djkurran@ucalgary.ca).

studies of excised tissues have demonstrated a wide range of breast tissue properties, with increasing permittivity and conductivity noted with a decrease in the proportion of adipose tissue [3]. Microwave-frequency approaches to imaging the complex distribution of electromagnetic properties in the breast include tomography and radar-based imaging. On one hand, microwave tomography uses measured microwave scattering data to produce quantitative images of the breast's dielectric property profile. Methods reported in [4, 5] are targeted at early stage breast cancer screening, while in [6] a clinical system has been developed for breast cancer treatment monitoring. On the other hand, radar-based imaging illuminates the breast with an ultrawideband (UWB) pulse of electromagnetic energy from sensors positioned at multiple locations around the breast. Signal processing algorithms are applied to the pre-conditioned reflected signals to produce a backscatter energy map related to locations where differences in tissue properties occur. Initial pre-clinical testing of this technique has been recently reported in [7, 8].

Both radar-based and microwave tomography imaging face significant challenges. For example, radar-based imaging techniques typically make an *a priori* assumption about the average relative permittivity value for the entire breast volume when creating the backscatter energy images. However, the breast has a complicated structure, leading to significant variability in the propagation speed of the electromagnetic energy travelling through tissue. Microwave tomography reconstructs the dielectric properties of an object by using an objective function to measure the discrepancy between the measurements and fields generated by a numerical simulation of the system (i.e., a forward solver) [9–11]. The complex nature of the internal breast structure, the lack of *a priori* information about the internal structure, and limitations in the quality and quantity of the measurement data lead to an inverse scattering problem that is nonlinear, non-convex, and severely ill-posed. Both tomography and radar-based imaging would benefit from estimates of the skin thickness, as well as the locations of regions dominated by adipose and fibroglandular tissues.

A class of microwave tomographic approaches to estimating the location of interfaces between regions has been reported at microwave frequencies. These approaches may be categorized as shape-optimization techniques. For example, an approach that integrates a multi-scaling procedure and the level-set-based optimization technique is presented in [12, 13] and is used for the shape reconstruction of multiple and disconnected homogeneous scatterers. The feasibility of the technique to detect unknown anomalies (e.g., cracks) in dielectric materials is evaluated in [14]. The application of shape-optimization techniques to numerical and experimental data for microwave imaging of perfect electric conductor objects is presented in [15, 16], respectively. A similar approach is also proposed for microwave breast imaging (see [4] or [17] for examples). Like other microwave tomographic techniques, these shape-optimization approaches face significant computational and mathematical challenges since the objective functional is nonlinear (i.e., it has multiple solutions), the problem is severely ill-posed, and the contour information is extracted from the transmission data using only a few frequencies.

In this paper, we present a technique that may be applied to backscattered microwave data collected from an object to extract spatial features associated with interfaces enclosing regions of dissimilar properties. The distinguishing feature of the technique that we are presenting is that efficient evaluation of the skin thickness and contour samples may be achieved directly from UWB reflection data. In [18], we presented a technique adapted for near field applications which we refer to as the *reflection data decomposition* (*RDD*) *algorithm*. This algorithm estimates the TOA and scaling factor of the reflections (relative to a reference function) that arise from dielectric property changes within an object, and has been tested on planar structures. In this paper, we adapt the RDD algorithm to incorporate *a priori* information about the geometric and/or dielectric properties of a region, as well as information collected at different frequency bands. The TOA information is also transformed to an estimate of the thickness of regions and locations of points on contours that segregate regions of dissimilar dielectric properties. Section 2 describes both of these methods in more detail. The algorithms are applied to 2D numerical models of increasing complexity in Section 3, demonstrating accuracy with differences between the models used to generate the reference function and the test data, as well as robustness to variations in layer thicknesses and shapes. Finally, the algorithms are applied to breast models based on MR scans in Section 4, suggesting the feasibility of delineating regions dominated by fat and glandular tissues.

2. METHODS

We begin with a general description of the problem. Consider an inhomogeneous dielectric object S shown in Fig. 1 covered by a thin layer which we denote as region 1 (Σ_1). The interior consists of two regions, labeled Σ_2 and Σ_3, having dissimilar dielectric properties. We position the object within a bounded 2D homogenous measurement

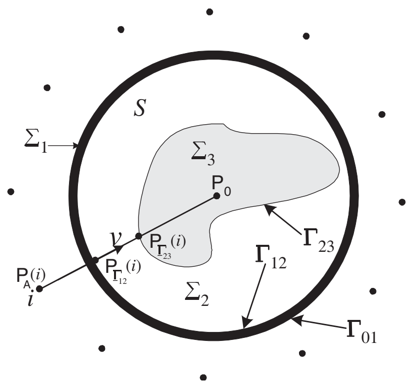

Figure 1. A region Ω with known dielectric properties is bounded by N sources/sensors (dots) co-located on its boundary $\partial\Omega$. Contained within the measurement region is a dielectric object S covered by a thin layer (Σ_1) with ϵ_{r1}, σ_1. The interior of the object has two regions (Σ_2, Σ_3) with dissimilar properties ϵ_{r2}, σ_2 and ϵ_{r3}, σ_3, respectively. The problem considered here is to evaluate points $P_{\Gamma_{12}}(i)$ and $P_{\Gamma_{23}}(i)$ on contours Γ_{12} and Γ_{23}, respectively.

region, Ω. The interfaces between regions are denoted as Γ_{01}, Γ_{12} and Γ_{23}, respectively. We note that for the breast imaging application, region 1 represents skin, while regions 2 and 3 represent regions dominated by adipose and glandular tissues, respectively. These interior regions are not restricted to be homogeneous, but rather represent regions that are dominated by a particular tissue type.

A source element illuminates Ω with an UWB electromagnetic pulse, while the sensor at the same location as the source records the backscattered signals. A full set of data collection using this configuration consists of moving the source and sensor pair to N equally spaced locations on the boundary of the measurement region. The locations of the sensors and contour Γ_{01}, as well as the dielectric properties of region Ω are known *a priori*. Furthermore, we assume that the relative permittivity of regions 1 and 2 are estimated using a technique such as the layer stripping approach presented in [19] or [20].

For each sensor, the reflected field information is used to estimate the points $P_{\Gamma_{12}}(i)$ and $P_{\Gamma_{23}}(i)$ on contours Γ_{12} and Γ_{23}, respectively. Repeating this procedure for N sensors leads to a sequence of points which we refer to as contour samples that may be used to estimate contours Γ_{12} and Γ_{23}. The methodology we have developed to identify the reflection that arises from each interface is described in Subsection 2.1. Each reflection is characterized by its scaling factor and TOA. The TOA is used to estimate the location on the contour from which the reflection originated, as described in Subsection 2.2.

2.1. Estimating Amplitude and TOA of Each Reflection

The object in Fig. 1 is illuminated by an UWB pulse and a single sensor receives the reflected signal. The data received by the sensor are conditioned so that the transmitted signal is removed from the reflection data. The pre-conditioned data, $y(t)$, are modeled as a superposition of scaled and delayed replicas of a reference signal $r(t)$ plus noise:

$$y(t) = \sum_{m=1}^{M} \alpha_m r(t - \tau_m) + e(t), \qquad 0 \leq t \leq T \tag{1}$$

where M is the number of replicas of $r(t)$; α_m and τ_m are the scaling factor and TOA of the mth replica, respectively; T is the duration of the signal; and $e(t)$ is noise modeled as a zero-mean Gaussian random process. Each of the scaled and time-delayed versions of the reference signal represent a reflection from an interface separating the object's different dielectric regions, so the TOA information may be used to imply the location of these interfaces and the extent of each region.

The approach to extracting the scaling factors and TOAs from a given backscattered signal is detailed in [18]. If *a priori* information is available about the geometric properties of a region (e.g., the skin layer thickness and/or properties), then this information may be incorporated into the reference signal used in (1) to improve the model of the reflection and the accuracy of parameter estimates. For example, simulations of a model or measurements of a test object may be used to generate reference reflections. The model may be updated to include *a priori* information, resulting in multiple reference functions that correspond to e.g., reflections from the exterior and interior of the skin layer. To accommodate *a priori* information, we adapt the RDD algorithm to use multiple reference functions to estimate reflections contained in the recorded data using the three step procedure shown in Fig. 2.

The multiple reference function approach may also be used to accommodate reference functions with different frequency contents. For example, when imaging the breast at microwave frequencies, the spectral content of the illuminating signal is an important consideration. On the one hand, an illuminating signal with higher frequency components ($\approx$ 12.5 GHz) is required to resolve the skin thickness. However, higher losses at these frequencies lead to poor depth of penetration, so the use of this signal is restricted to extracting information related to thin structures close to the surface (e.g, the skin). On the other hand, identifying interfaces deeper within the breast requires an illuminating signal with lower frequency components in order to improve the depth of penetration. Unfortunately, the improvement in depth of penetration of the signal comes at the expense of loss of resolution. Therefore, we propose a sequential estimation procedure that preserves resolution while enhancing penetration. The object is first illuminated with a signal having higher frequency components, $x_{fh}(t)$. Reference functions are also generated for this signal and are used to decompose the reflections contained in the backscattered data. The TOA estimates for the first two reflections are used to evaluate the skin thickness. Next, an illuminating signal, $x_{fl}(t)$, with frequency components lower than the first illuminating signal is used. The decomposition procedure is reapplied to the backscattered data using reference signals generated for this second excitation. The TOA for the second and third reflections are used to estimate the distance from contour Γ_{12} to Γ_{23}.

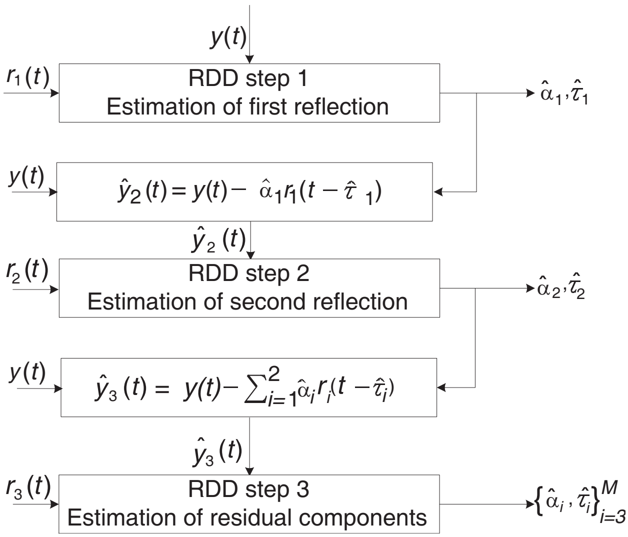

Figure 2. Flow-chart of the three-step procedure used to estimate the scaling factor α and TOA parameter τ for each reflection contained in the backscattered data $y(t)$ recorded by a sensor. At each step, *a priori* information about a region (e.g., geometrical and/or dielectric properties) may be incorporated into the reference signal $r_i(t)$ used by the reflection data decomposition algorithm.

2.2. Estimating Amplitude and TOA of Each Reflection

Once the recorded reflection signal is decomposed into M components, estimates of the TOAs and scaling factors of the reflections that arise from each interface are available. This information is first used to estimate the extent of each region near each antenna. The estimates from all sensors are then used to identify points on contours separating the regions.

The TOA is used to estimate the thickness or extent of each region with the assumption that the average permittivity of each region is known. For sensor i, the extent of region j is estimated using the difference in TOA between successive reflections:

$$\Delta\tau_j(i) = \tau_{j+1}(i) - \tau_j(i). \tag{2}$$

Specifically, the thickness of layer j near antenna i, $\widehat{w}_j(i)$, is estimated as:

$$\widehat{w}_j(i) = \frac{\Delta\tau_j(i) c_0 10^3}{2\sqrt{\widehat{\epsilon}_{rj}}} \qquad \text{(mm)} \tag{3}$$

where $c_0 = 2.9979 \times 10^8$ m/s is the speed of light in free space and $\widehat{\epsilon}_{rj}$ is the estimated average relative permittivity of the jth region of interest.

Next, an iterative procedure uses the layer thicknesses in conjunction with a line-of-sight ray connecting the sensor to the center of the region of interest (ROI). The center of the ROI is identified as point P_0. The location of sensor i is known and described as point $P_A(i)$ with $P_{A,z}(i)$ and $P_{A,y}(i)$ denoting the z and y-coordinates, respectively. The distance from the ith antenna to the outer surface of the object, $w_0(i)$, is also assumed to be known *a priori*.

Consider the contour separating regions 1 and 2 (Γ_{12}). The distance from antenna i to a point on this contour is given by:

$$\widehat{w}_{\Gamma_{12}}(i) = w_0(i) + \widehat{w}_1(i). \qquad \text{(mm)} \tag{4}$$

This distance is used to estimate the coordinates of the point $P_{\Gamma_{12}}(i)$ on the contour. As shown in Fig. 1, a line-of-sight ray connects the ith sensor at point $P_A(i)$ with the center of the ROI at point P_0. A direction vector $\vec{v}$ along the ray points to the center and is incorporated into the vector parametric equation of the ray:

$$\vec{P}_{\Gamma_{12}}(i) = \vec{P}_{\Gamma_A}(i) - t\vec{v} \tag{5}$$

where $\vec{P}_{\Gamma_{12}}(i)$ is the position vector of the point $P_{\Gamma_{12}}(i)$ on the contour, $\vec{P}_A(i)$ is the position vector of the location of the ith antenna, and

$t \in [0,1]$. When $t = 0$, $P_{\Gamma_{12}}(i) = P_{\Gamma_A}(i)$; when $t = 1$, $P_{\Gamma_{12}}(i) = P_0$. The expression given by (5) is constrained by

$$\widehat{w}_{\Gamma_{12}}(i) = \sqrt{(P_{A,z}(i) - P_{\Gamma_{12,z}}(i))^2 + (P_{A,y}(i) - P_{\Gamma_{12,y}}(i))^2} \tag{6}$$

where $P_{\Gamma_{12,z}}(i)$, $P_{\Gamma_{12,y}}(i)$ are the z and y-coordinates of $P_{\Gamma_{12}}(i)$, respectively. The coordinates of $P_{\Gamma_{12}}(i)$ are determined iteratively using (5) and (6) with the following procedure. Scalar t is incrementally increased to move the position vector point $\vec{P}_{\Gamma_{12}}(i)$ along the line-of-sight ray given by (5) until the distance traveled by the point satisfies the distance given by (6). This process is repeated for all N sensors in order to form a sequence of points $P_{\Gamma_{12}}(1), \ldots, P_{\Gamma_{12}}(N)$ which estimate N locations along the contour Γ_{12}.

We repeat this process to determine the coordinates of the point $P_{\Gamma_{23}}(i)$ on the estimated location of contour Γ_{23}. In this case, the distance from antenna i to a point on the contour Γ_{23} is estimated with

$$\widehat{w}_{\Gamma_{23}}(i) = \widehat{w}_{\Gamma_{12}}(i) + \widehat{w}_2(i). \qquad \text{(mm)} \tag{7}$$

We refer to this entire procedure as the *contour sample evaluation algorithm*. The sequence of $2N$ points may be used to infer the basic shapes of contours Γ_{12} and Γ_{23} (i.e., geometrical properties) and of the object's interior regions. Hence, this information may be used to approximate the object's internal structure. Although we restrict this technique to the identification of just three regions for this investigation, it can be easily extended to extract contour information related to more than three regions.

3. INITIAL PERFORMANCE EVALUATION

The ability of the algorithm to extract an object's internal geometrical properties is evaluated with a 2D object having progressively more complex regional shapes. Furthermore, the results are compared as more *a priori* information about the regional properties is incorporated into the reference signals. The approach used to generate the numerical data and the metrics used to evaluate the performance of the algorithm are described in Subsections 3.1 and 3.2, respectively. The results and performance of the algorithm are described in Subsection 3.3.

3.1. Generation of Numerical Data

Numerical simulations using the finite difference time domain ($FDTD$) method are used to generate test data. In these examples, the $FDTD$ problem space is bounded by a five-cell thick perfectly matched layer

(PML) boundary (4th order, $R(0) = 10^{-7}$) with spatial grid resolution of 0.5 mm. Similar to the illustration in Fig. 1, a model having three distinct homogeneous regions is placed within the problem space and the sensor and source are co-located 10 mm from the surface of the outer layer. Both the model and source/sensor are located in free space. An impressed current source is used in these TM_x simulations. The model is illuminated with an UWB differentiated Gaussian pulse. The maximum frequency $f_{\max}$ of the pulse is defined as the frequency at which the magnitude of the spectrum is 10% of the maximum. The number of samples is $N = 4000$, and the sample time is $T_S = 1.06$ ps.

When generating the numerical data, reflections are recorded as the sensor is scanned to 20 equally spaced locations around the model. The transmitted signal is acquired by carrying out a simulation without the model. Data received by the sensor are conditioned such that the transmitted signal is removed from each reflection. The data are then normalized to the reflected signal's maximum positive value and are contaminated with 20 dB of white Gaussian noise.

3.2. Assessing the Performance of the Algorithm

To assess the performance of the contour sample evaluation algorithm, the actual reflections from each of the three interfaces (Fig. 1) are isolated in order to extract actual values of the scaling factors and TOAs. First, a simulation is carried out with a homogeneous model (i.e., entire model has the same properties as the outer layer) to provide an isolated version of the reflection from the first interface, $y_1(t)$. The reflection is normalized by the positive maximum of the reflection, then characterized by the scaling factor, $\alpha_1 = 1.0$, and TOA τ_1 which is the time that the positive maximum occurs. Next, a simulation is carried out with the third region replaced with a dielectric material having the same properties as the second region and this signal is used to isolate the reflection from the second interface, $y_2(t)$. After normalizing to the first reflection, the scaling factor α_2 and TOA τ_2 are determined. Finally, a third simulation is carried out with the three region model. The first two reflections are subtracted from the resulting data, isolating the reflection from the third interface, $y_3(t)$. After normalizing to the first reflection, the resulting signal is characterized by the scaling factor α_3 and TOA τ_3.

The error in TOA is explored by comparing actual and estimated differences in successive TOA estimates. Specifically, the error, $\Delta\tau_e(i)$, is calculated by subtracting the actual from the estimated $\Delta\tau(i)$ of the reflections. Rather than examining the error in TOA directly, the spatial error, $\Delta w_{ej}(i)$, for the jth layer is of greater practical interest and is calculated using

$$\Delta w_{ej}(i) = \frac{\Delta\tau_e(i)c_0 10^3}{2\sqrt{\epsilon_{rj}}} \qquad \text{(mm)} \qquad \text{for } j = 1, 2 \tag{8}$$

where ϵ_{rj} is the average relative permittivity of the jth layer. The thickness error for the jth layer is then calculated relative to the actual layer thickness. Likewise, the relative error for each of the reflection amplitudes is computed using

$$\alpha_{ej}(i) = \frac{\widehat{\alpha}_j(i) - \alpha_j(i)}{|\alpha_j(i)|} \qquad \text{for } j = 1, 2 \tag{9}$$

where $\widehat{\alpha}_j(i)$ is the estimated value of the jth scaling factor.

The similarity between the estimate of a reflection, $\widehat{y}_j(i)$, and the actual reflection is computed using:

$$\rho_j = \frac{\widehat{\mathbf{y}}_j^T \mathbf{y}_j}{\|\widehat{\mathbf{y}}_j\| \|\mathbf{y}_j\|} \qquad \text{for } j = 1, 2, 3. \tag{10}$$

A value close to 1 indicates a close similarity between the estimate of the reflection and the actual reflection.

Each performance measure is averaged over all N sensors.

3.3. Results

We first evaluate the performance of the algorithm for a base-line case whereby the object has a simple cylindrical shape and limited *a priori* information about the object is available. The same reference signal is used for all three steps of the parameter estimation algorithm and results are described in Subsubsection 3.3.1. The case where *a priori* information about both the thickness and dielectric properties of the outer layer (skin region) is used to refine the second reference signal is described in Subsubsection 3.3.2. Finally, the performance of the algorithm is evaluated when the skin region and the object's interior have more complicated geometrical properties in Subsubsections 3.3.3 and 3.3.4, respectively.

3.3.1. Case 1: Object with Simple Cylindrical Shape

A three layer cylinder is used to evaluate the effectiveness of the contour sample evaluation algorithm for an object with a geometrically simple internal structure. The model is shown in Fig. 3. Region 1 is a simplified representation of skin and will be referred to as the skin layer. The cylinder is illuminated with an UWB differentiated Gaussian pulse having a −3 dB bandwidth of 4.62 GHz (1.62–6.24 GHz). The maximum frequency $f_{\max}$ of the pulse is 8.59 GHz.

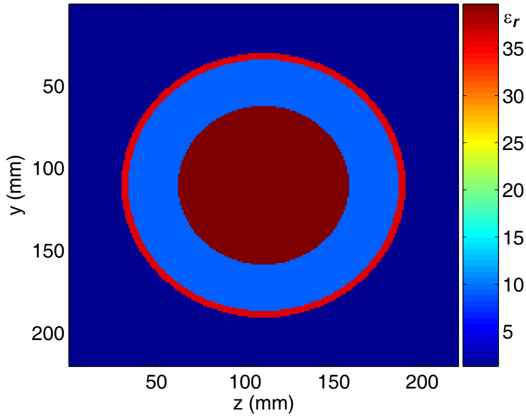

Figure 3. Relative permittivity profile of model 1. The skin layer is 2 mm thick with $\epsilon_{r1} = 36.0$, $\sigma_1 = 4.0\,\mathrm{S/m}$; the middle layer is 14 mm thick with $\epsilon_{r2} = 9.0$, $\sigma_2 = 0.4\,\mathrm{S/m}$; and the center layer is 24 mm thick with $\epsilon_{r3} = 40.0$, $\sigma_3 = 3.2\,\mathrm{S/m}$.

Table 1. Effect that the reference signal has on the quality of the parameter estimation for model 1. The performance measures are averaged over all 20 antennas.

Ref. Slab prop.		Δw_{e1}	Δw_{e2}	α_{e1}	α_{e2}	ρ_1	ρ_2	ρ_3
ϵ_r	σ (S/m)	mm/(%)	mm/(%)	(%)	(%)			
36	4	0.12 (6%)	−0.01 (−0.1%)	0.8	−0.4	0.9996	0.9419	0.7078
43.2	4.8	0.11 (6%)	−0.003 (−0.02%)	0.8	−4.2	0.9996	0.9415	0.7119
28.8	3.2	0.11 (6%)	0.007 (0.05%)	0.8	−3.6	0.9996	0.9417	0.7048

To test algorithm's robustness to variations between the reference signal and model, several scenarios are investigated. First, the reference signal is acquired by simulating a homogeneous planar layer (slab) having dielectric properties of $\epsilon_r = 36.0$, $\sigma = 4.0\,\mathrm{S/m}$. Next, reference signals are constructed using reflections from dielectric slabs with properties of $\epsilon_r = 28.8$, $\sigma = 3.2\,\mathrm{S/m}$ (i.e., the dielectric properties of the slab are −20% of the actual properties), and $\epsilon_r = 43.2$, $\sigma = 4.8\,\mathrm{S/m}$ (i.e., the dielectric properties of the slab are +20% of the actual properties). For these cases, the reflection from the slab is normalized and used for all three reference signals shown in Fig. 2.

Table 1 summarizes the results obtained for each of the three reference signals. First, we examine the average error of the skin layer thickness, Δw_{e1}, and the average error in the skin-to-region 3 distance, Δw_{e2}. These errors are very small for all cases, suggesting that the algorithm is able to accurately estimate the TOA for the first three reflections and that this estimation is robust to differences in dielectric properties between the slab used to obtain the reference signal and the object under test. These results are consistent with the findings presented in [18]. Furthermore, we note that the reference signal is constructed using the reflection from a dielectric slab; but the actual reflections arise from cylindrical objects. This means that the estimation procedure is also robust to geometrical differences between the object used to generate the reference signal and the actual contours of the object from which the reflections arise.

The results shown in Table 1 also suggest accurate estimation of the scaling factor for the first two reflections. This estimation is also robust to a discrepancy between the dielectric properties of the slab used to obtain the reference signal and the actual dielectric properties of the model. We note that accurate estimation of the scaling factor of the first two reflections is of practical importance since these estimates may be used by a layer stripping method (e.g., as suggested by [19]) to estimate the relative permittivity of the skin and region 2.

For the reference signals tested, the average similarity measure between the estimate of the first reflection and the actual reflection, ρ_1, suggests that the first reflection is modeled accurately. The average value of the similarity measure given by ρ_2 implies a deterioration of the model for the second reflection. This, in turn, leads to unwanted artifacts in the residue after the skin response is removed from the signal, resulting in the deterioration of the estimation of the third reflection and decline in the average similarity measure ρ_3. However, the deterioration in the accuracy of the estimation of these two reflections does not appear to affect the accuracy of the estimation of the TOA parameters.

The contour samples are evaluated for Γ_{23} when the algorithm uses a single reference signal constructed from the reflection off of a dielectric slab with $\epsilon_r = 43.2$, $\sigma = 4.8\,\mathrm{S/m}$. The results are shown in Fig. 4 and demonstrate that for this simple shape, the geometric properties of region 3 are accurately extracted and support the results in Table 1.

3.3.2. Case 2: Incorporating Additional a Priori Information

Model 1 is used to investigate if there is an improvement in the quality of the estimates if additional *a priori* information about the skin layer

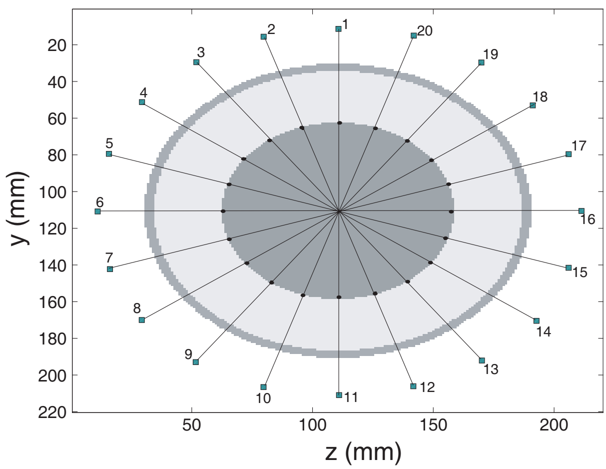

Figure 4. Contour samples (dots) evaluated for contour Γ_{23} when the algorithm uses a single reference signal constructed from the reflection off of a dielectric slab with $\epsilon_r = 43.2$, $\sigma = 4.8\,\mathrm{S/m}$. The ith contour sample $P_{\Gamma_{23}}(i)$ is evaluated from the reflection data $y(t)$ recorded by the ith sensor (rectangle) with the procedure described in Subsection 2.2 which uses the line-of-sight rays shown connecting each sensor with the center of the model.

is incorporated into the estimation procedure. In particular, we assume that information about both the skin layer's thickness and dielectric properties is available and used to construct a signal for the second reference.

To acquire the second reference signal, $r_2(t)$, a simulation is carried out with a 2 layer slab. A thin outer layer covers a second layer with dielectric properties of $\epsilon_r = 9.0$, $\sigma = 0.4\,\mathrm{S/m}$. Several versions of these reference signals are obtained by using thin layers with dielectric properties of $\epsilon_r = 28.8$ $\sigma = 3.2\,\mathrm{S/m}$, $\epsilon_r = 36.0$ $\sigma = 4.0\,\mathrm{S/m}$, $\epsilon_r = 43.8$ $\sigma = 4.8\,\mathrm{S/m}$. For a set of dielectric properties, three thicknesses of 1 mm, 2 mm, or 3 mm are simulated. Therefore, a total of 9 sets of reference signals are developed. A slab with the same properties as the thin layer is used to generate the reflection from the first interface, $r_1(t)$. This reflection is subtracted from the reflection from the thin slab in order to isolate the reflection from the second interface. The subtracted signal is then normalized to the first reference signal and used as the second reference signal, $r_2(t)$. Finally, we use the first reference signal for $r_3(t)$.

Table 2 summarizes the performance of the algorithm with the

Table 2. Effect that the reference signal has on the quality of the parameter estimation for model 1. The performance measures are averaged over all 20 antennas.

Ref. slab prop.			Δw_{e1}	Δw_{e2}			
thickness (mm)	ϵ_r	σ (S/m)	mm/ (%)	mm/ (%)	ρ_1	ρ_2	ρ_3
1	36.0	4.0	0.03 (1.5%)	0.00 (0.0%)	0.9996	0.9966	0.8635
1	43.2	4.8	0.05 (2.15%)	−0.07 (−0.5%)	0.9996	0.9969	0.8807
1	28.8	3.2	0.04 (2.0%)	0.02 (0.14%)	0.9996	0.9958	0.8690
2	36.0	4.0	0.04 (2.0%)	−0.02 (−0.14%)	0.9996	0.9882	0.8036
2	43.2	4.8	0.02 (1.0%)	0.08 (0.57%)	0.9996	0.9883	0.7800
2	28.8	3.2	0.09 (4.5%)	−0.06 (−0.43%)	0.9996	0.9961	0.7782
3	36.0	4.0	0.09 (4.5%)	−0.16 (−1.14%)	0.9996	0.9915	0.8858
3	43.2	4.8	0.08 (4.0%)	−0.09 (−0.64%)	0.9996	0.9870	0.8601
3	28.8	3.2	0.10 (5.0%)	−0.26 (−1.86%)	0.9996	0.9946	0.9224

9 reference signals. The results indicate that the skin thickness is estimated more accurately compared to Table 1 (single reference signal), although the difference in the error is not significant. However, the results also suggest that there is no noticeable improvement in the accuracy of the estimation of the skin-to-region 3 distances when the two different reference signals are used. The results do not significantly change with variations to the thickness and properties of the slab used to generate the second reference signal. Finally, we note that the scale factor for reflection 1 is estimated with 0.8% error in all cases, while the magnitude of the error in the scale factor for reflection 2 is less than 6% for all cases.

The similarity measure between the estimate of the second reflection and the actual second reflection indicates a significant improvement compared to the single reference signal in Subsubsection 3.3.1.

The first two reflections collectively represent the skin response. The average values of both similarity measures (ρ_1 and ρ_2) indicate that the skin response is accurately estimated when using a second reference signal. These results are maintained when various thicknesses and dielectric properties of the slab are used to construct the two reference signals. This is of practical importance since an accurate estimation of the skin response may be used to reduce the skin reflection [21]. Moreover, accurate estimation of the skin response is important for the reduction of artifacts in the residual signal. The reduction of these artifacts is suggested by the improvement in the similarity between the estimation of and the actual third reflection compared to Table 1 where only a single reference signal is used.

3.3.3. Case 3: Irregularly-shaped Regions

Two models are used to explore cases where the regions do not have uniform thicknesses or regular shape. Model 2, shown in Fig. 5, has a non-uniform skin layer with asymmetrical shape. It is used to evaluate the effect that the shape and variable thickness of the skin layer have on the estimation procedure. The average thickness of the skin layer is 2.12 mm and its dielectric properties are homogeneous with $\epsilon_{r1} = 36.0$, $\sigma_1 = 4.0\,\mathrm{S/m}$. Model 3 is used to examine the effect of the shape of region 3. This model has the same skin layer as model 2 and the properties of the three layers are also the same, however region 3 has 4 lobes (see Fig. 6). For both models, a single reference signal is constructed using the procedure described in Subsubsection 3.3.1 from the reflection off of a dielectric slab with $\epsilon_{r1} = 37.4$, $\sigma_1 = 4.2\,\mathrm{S/m}$.

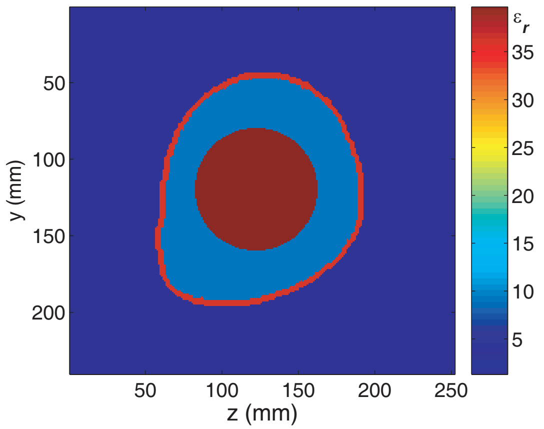

Figure 5. Relative permittivity profile for model 2.

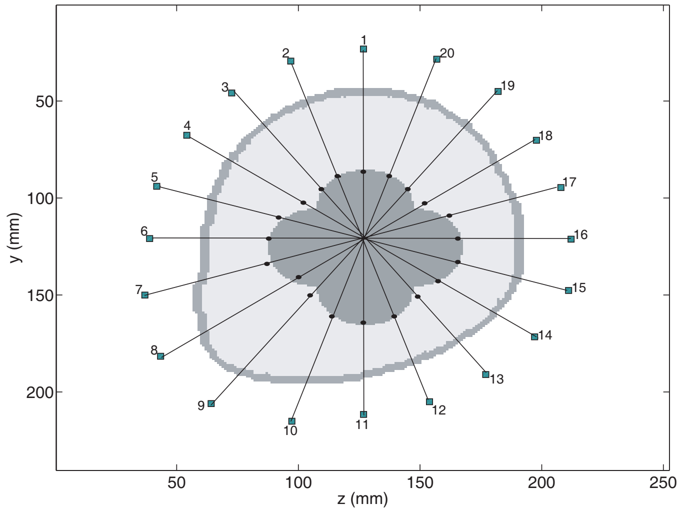

Figure 6. Contour samples (dots) evaluated for contour Γ_{23} of model 3 when the algorithm uses a single reference signal constructed from the reflection off of a dielectric slab with $\epsilon_r = 37.4$, $\sigma = 4.2\,\mathrm{S/m}$.

For model 2, the skin layer thickness and the skin-to-region 3 distances are evaluated using (2). The average error for the estimated skin layer thickness is 0.08 mm (relative error is 3.8%) and the average error for the estimated skin-to-region 3 distance is −0.012 mm. The results indicate that the estimation technique accurately estimates these distances and is robust to variations in the shape and thickness of the skin layer. Next, the contour samples $P_{\Gamma_{23}}(i)$ for $i = 1$ to 20 are evaluated using (2)–(6). Although a plot of the contour samples for model 2 is not shown, we note that precise sampling of the contour is achieved and that the results have accuracy very similar to what is shown in Fig. 4. This is supported by the fact that the average difference in distance the model 2 contour samples are from the actual interface is less than 0.02 mm.

For model 2, the results obtained using a single reference signal are compared to those obtained when the two reference signals are acquired using a 3 mm slab with $\epsilon_r = 37.4$, $\sigma = 4.2\,\mathrm{S/m}$. The average error for the estimated skin layer thickness is −0.11 mm (or a relative error of 4.9%) and the average error for the estimated skin-to-region 3 distance is −0.132 mm. This implies that there is not a significant difference in the distance estimates, even if more *a priori* information is used for the skin. This result supports the findings in Subsubsection 3.3.1.

For model 3, the average error for the estimated skin layer thickness is 0.09 mm (relative error is 4.24%) and the average error for the estimated skin-to-region 3 distance is -0.68 mm. Next, the contour samples $P_{\Gamma_{23}}(i)$ for $i = 1$ to 20 are evaluated using (2)–(6) and are superimposed onto the model in Fig. 6. From Fig. 6, we observe that the accuracy of the skin-to-region 3 distance estimation varies depending on the sensor location. The line-of-sight ray for sensors 1 and 2 shown in Fig. 6 intersect region 3 at a location where the contour has a convex shape. The line-of-sight ray for sensors 4 and 9 intersect region 3 at a location where the shape is concave. For the later scenario, we hypothesize that multiple reflections arise from the expanding transmitting signal as it interacts with the contour at multiple locations. This leads to an underestimation of the contour sample and demonstrates a shortcoming of the line-of-sight approach. In general, the method is unable to accurately extract detailed spatial features related to concave regions.

4. APPLICATION OF ALGORITHM TO 2D NUMERICAL BREAST MODELS

The ability of the algorithm to accurately sample the outline of a contour separating regions having dissimilar dielectric properties was demonstrated in Section 3. We now apply this tool to a more practical but challenging problem in which the goal is to use the reflection data recorded by the sensors to evaluate the location of various interior contours in order to infer the internal structure of a breast. For this investigation, we assume that the breast consists of an outer skin layer and an interior consisting of two regions: a fat region dominated by adipose tissue and a glandular region dominated by fibroglandular tissue. Referring to Fig. 1, the fat region corresponds to region 2 and the glandular region corresponds to region 3. For application to a realistic breast model, regions 2 and 3 are not assumed to be homogeneous.

The accuracy and performance of the algorithm in this practical scenario is investigated using numerical breast models constructed from coronal MR scans acquired from two different patients as part of a patient study described in [22]. The MR scan is collected prior to injection of a contrast agent used routinely in MR and construction of the numerical models follows a three step procedure described in [23]. First, the breast location is defined and a non-uniform skin layer is added. Next, the breast interior is segmented into 5 tissues. Mapping of MR pixel intensity to breast tissue electrical properties employs a piecewise linear mapping by assigning ranges of pixel intensities to each of the tissue groups defined in [3]. Model 5 contains a tumor extracted from images acquired after a contrast agent is administered

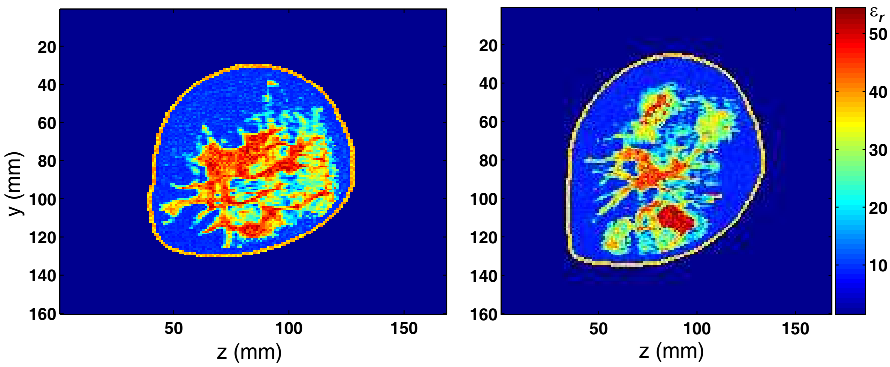

Figure 7. Relative permittivity profiles for models 4 (a) and 5 (b) each constructed from an MR coronal slice.

to the patient and inserted into the numerical breast model at the appropriate location. To further model anatomical heterogeneity of the biological tissue, we introduce random perturbations of $+/-10\%$ around the dielectric property values for the tissue types. The relative permittivity profiles of models 4 and 5 are shown in Fig. 7 and illustrate the anatomically realistic variations of the dielectric properties which have been derived from the MR scans of two different patients. For model 4, the actual skin thickness varies from 1.71 to 3.00 mm and the mean thickness is 2.12 mm; the spatial average of the dielectric properties over the skin region are $\epsilon_{r1} = 36.2$ $\sigma_1 = 3.99\,\mathrm{S/m}$; and the spatial average of the dielectric properties over the adipose region are $\epsilon_{r2} = 9.61$, $\sigma_2 = 0.33\,\mathrm{S/m}$. For model 5, the actual skin thickness varies from 1.91 to 2.54 mm and the mean thickness is 2.23 mm; the spatial average of the dielectric properties over the skin region are $\epsilon_{r1} = 36.05$ $\sigma_1 = 4.01\,\mathrm{S/m}$; and the spatial average of the dielectric properties over the adipose region are $\epsilon_{r2} = 10.11$, $\sigma_2 = 0.46\,\mathrm{S/m}$.

Simulations with the $FDTD$ method are used to generate test data. In these examples, the $FDTD$ problem space is bounded by a five-cell thick perfectly matched layer (PML) (4th order, $R(0) = 10^{-7}$), and consists of 160×168 cells with spatial grid resolution of 1 mm. A source and sensor are co-located 10 mm from the outer skin surface of the model. Both the breast and source/sensor are immersed in free space. The source and sensor are sequentially positioned to 40 equally spaced locations around the breast and simulations are performed at each location. An impressed current source is used in these TM_Z simulations. The number of samples is $N = 4000$, and the sample time is $T_S = 2.12\,\mathrm{ps}$.

The multi-frequency strategy is used to estimate the locations of the fat and glandular regions in breast model 4. Therefore, two sets of data are collected. First, the breast is illuminated with an UWB differentiated Gaussian pulse having a -3 dB bandwidth (BW) of 4.62 GHz (1.62–6.24 GHz). The maximum frequency $f_{\max}$ of the pulse is 8.6 GHz. A second set of data are collected when the breast is illuminated with a differentiated Gaussian pulse with a -3 dB bandwidth of 2.57 GHz (0.92–3.49 GHz) and $f_{\max}$ is 4.8 GHz. Data recorded by the sensors are conditioned so that the transmitted signal is removed from each reflection. The data are then normalized to the reflected signal's maximum positive value. Similar to the first part of this study, the data are contaminated with 20 dB of white Gaussian noise.

For this example, two reference signals are acquired using a 3 mm slab with $\epsilon_{r1} = 37.8$, $\sigma_1 = 4.2$ S/m. We justify using two different reference signals since the breast skin thickness is typically between 0.7 and 2.3 mm [24]. One set of reference signals is acquired when a 3 mm homogeneous dielectric slab is illuminated with the 4.62 GHz BW signal. The second set of reference signals are acquired when the slab is illuminated with the 2.57 GHz BW signal.

The skin thickness is evaluated using the data and reference signals with higher frequency components and the skin-to-region 3 distances are evaluated using the data and reference signals with lower frequency components. Using this approach, the thickness of the skin layer has an average error of 0.07 mm (or an average relative error of 3.3%), which is in agreement with the skin thickness estimation results presented in Subsubsection 3.3.3. That is, the algorithm is able to estimate the skin thickness accurately independent of the shape and internal structure of the breast.

The contour samples for Γ_{23} estimated from the skin thickness and skin-to-region 3 distance are superimposed on model 4 in Fig. 8. We observe that the method estimates locations that typically lie on or near the boundary between fatty and glandular tissues. Therefore, it appears that the method is able to extract general spatial features of the contour. However, the algorithm is unable to extract detailed features associated with small spatial oscillations of the contour (e.g., concave regions). Nevertheless, the result is of practical importance since the points may be used to form parametric models of the contour that segregate regions of the breast dominated by adipose and fibroglandular tissue.

For comparison, the Γ_{23} contour samples are evaluated without the multi-frequency approach for model 5. That is, similar to Section 3, the estimation procedure is carried out using only a single set of reference signals and data generated when using the 4.62 GHz BW excitation signal. Furthermore, we use the inverse tomographic method outlined in [25] to estimate the spatial average dielectric properties used in (2) over the skin and adipose regions. Specifically, the average relative permittivity evaluated over the skin and adipose regions are 36.90 and 8.63, respectively. The thickness of the skin layer has an average error of -0.05 mm (or an average relative error of -2.24%). The plot of the contour samples for this case is shown in Fig. 9. We observe that the results obtained using the single excitation approach are comparable to those obtained using multi-frequency strategy, i.e., the method is able to extract general spatial features of the contour. Regardless of the highly heterogeneous nature and complex shape of the fibroglandular region and the presence of isolated fibroglandular scatterers within the adipose region, the results support the feasibility of using the reflection data to extract information about the breast's internal structure. Furthermore, the results imply that the algorithm is

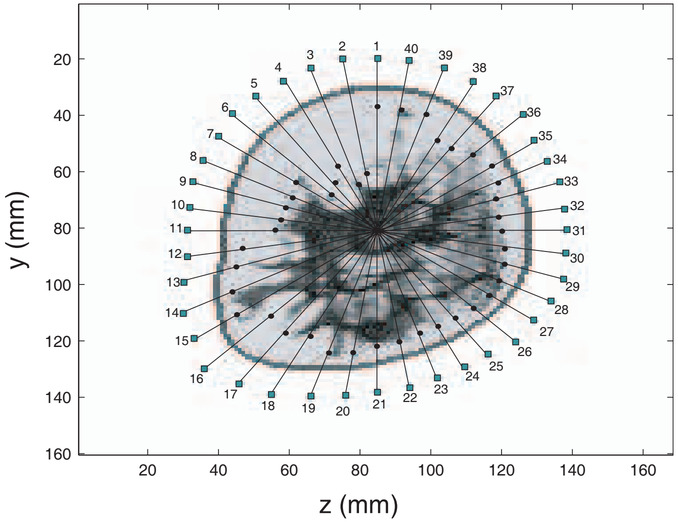

Figure 8. Contour samples (dots) evaluated for contour Γ_{23} of model 4 when the algorithm uses a two different reference signals constructed from the reflections off of a dielectric 3 mm slab with $\epsilon_r = 37.8$, $\sigma = 4.2$ S/m. Two sets of reference signals are acquired to implement the multi-frequency approach. One set of reference signals is acquired when a 3 mm homogeneous dielectric slab is illuminated with the 4.62 GHz BWsignal and a second set of reference signals are acquired when the slab is illuminated with the 2.57 GHz BW signal.

robust to uncertainty in knowledge of the average relative permittivity of the skin and adipose regions. The contour samples indicate that general regional features are extracted from the EM reflection data to allow the identification of the skin, adipose, and fibroglandular regions that dominate the object's underlying structure.

We anticipate that the advantages of using the multi-frequency approach may be fully realized when penetrating through tissues that have a greater conductivity than adipose tissue. For example, if there is a requirement to extract further contour shape information within higher loss region 3 (e.g., evaluate samples on a contour that enclose a tumor), then the use of the lower frequency excitation signals may assist to accomplish this. Likewise, the multi-frequency approach may also provide superior results over the single excitation signal approach if an excitation with a higher frequency content than used for this example is required. Finally, a possible third scenario in which the multi-frequency approach may be used is if the region of interest is small and a great distance from many of the sensors.

As indicated in the introduction, microwave tomography approaches (e.g., [9–11]) including the shape-optimization techniques (e.g., [12–17]) attempt to solve an inverse scattering problem that

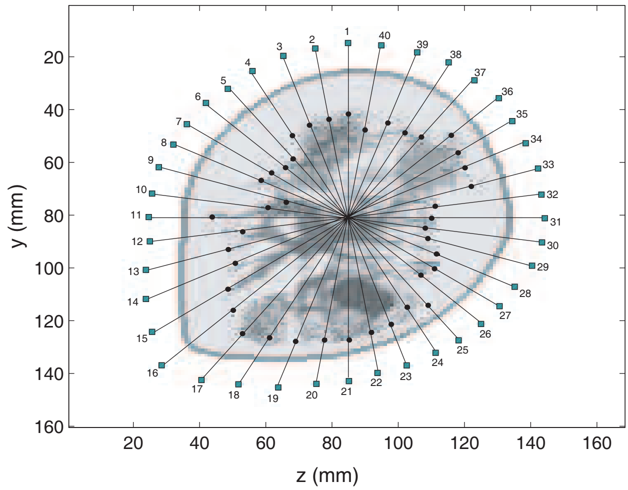

Figure 9. Contour samples (dots) evaluated for contour Γ_{23} of model 5 when the algorithm uses a two different reference signals constructed from the reflections off of a dielectric 3 mm slab with $\epsilon_r = 37.5$, $\sigma = 4.2\,\mathrm{S/m}$. Only one set of reference signals is acquired when a 3 mm homogeneous dielectric slab is illuminated with the 4.62 GHz BW.

is severely ill-posed and non-linear. The technique presented in this paper provides a direct, fast and efficient means to exploit information contained in the backscattered field data to help remedy these mathematical challenges. For example, the tomography techniques may be initialized with estimates of the locations and shapes of the contours evaluated from the reflection data, such as the information presented in Figs. 4, 6, 8 or 9. This *a priori* information may be used to improve the convergence behavior of these iterative reconstruction techniques (e.g., reduce the number of steps required to converge). The quality of the shape and dielectric property reconstructions may also be improved since this information may limit the risk of being trapped in false solutions which arise when solving the optimization problem. In a general setting, practical implementation of this integration (i.e., collecting the UWB reflection measurements to extract the contour samples and collecting the transmission measurements for tomography) may be achieved using an UWB measurement system described in [16], or [26, 27]. The UWB sensor and measurement system used for a patient study described in [22, 28], respectively, offer a practical means to integrate the radar and tomographic approaches for breast imaging. Furthermore, for the multi-scaling procedures indicated in [12–14], the contours estimated by this algorithm may be used identify a region of interest where unknown scatterers are found to be located. With this region of interest identified, the spatial resolution may be enhanced within this region.

5. CONCLUSION

We presented an adapted reflection decomposition algorithm that incorporates *a priori* information about an object, as well as data collected over different frequency bands. This algorithm was shown to estimate the location of interfaces with mismatches between the models used to generate data and reference signals, as well as in models with complex shapes.

For microwave breast imaging applications, *a priori* information was shown to improve the estimation of the skin response. This information may be used by radar approaches to subtract the skin response from the early-time scattered fields. Furthermore, information related to the adipose/fibroglandular interface may be used to reduce clutter contained in the reflection data.

We have also presented an estimation technique that provides a direct and quick means to evaluate a sequence of points on a contour separating regions of dissimilar dielectric properties. The points may be collectively used to extract spatial features of the contour in order to infer an object's internal structure. It is observed that the algorithm is unable to extract features associated with small oscillations of the contour. Instead, more general information about the contour's shape is provided. As microwave imaging is a low resolution technique, this general information is practically useful.

The sequence of contour points may be used to construct a parametric model of the contour which may be incorporated into a radar-based or microwave tomography algorithm to provide *a priori* information about an object's internal structure. We note that for this investigation we assume *a priori* knowledge of the spatial average of the breast and adipose regions. This assumption may be relaxed when the algorithm is incorporated into a microwave tomography algorithm to generalize the method.

REFERENCES

1. Brenner, R. J. and Y. Parisky, "Alternative breast-imaging approaches," *Radiol. Clin. N. Am.*, Vol. 45, 907–923, 2007.
2. Fear, E. C., "Microwave imaging of the breast," *Tech. in Cancer Res. and Treat.*, Vol. 4, 69–82, 2005.
3. Lazebnik, M., et al., "A large-scale study of the ultrawideband microwave dielectric properties of normal, benign and malignant breast tissues obtained from cancer surgeries," *Phys. Med. Biol.*, Vol. 52, 6093–6115, Oct. 2007.
4. Irishina, N., D. Alvarez, O. Dorn, and M. Moscoso, "Structural level set inversion for microwave breast screening," *Inverse Problems*, Vol. 26, 1–26, 2010.
5. Shea, J. D., P. Kosmas, B. D. Van Veen, and S. C. Hagness, "Contrast-enhanced microwave imaging of breast tumors: A computational study using 3D realistic numerical phantoms," *Inverse Problems*, Vol. 26, 1–22, 2010.
6. Meaney, P. M., et al., "Microwave imaging for neoadjuvant chemotherapy monitoring," *Proc. EuCAP*, 1–4, Nice, France, 2006.
7. Klemm, M., et al., "Clinical trials of a UWB imaging radar for breast cancer," *Proc. EuCAP*, 1–4, Barcelona, Spain, 2010.
8. Sill, J., et al., "Tissue sensing adaptive radar for breast cancer detection: Comparison of measured and simulated patient data," *2010 IEEE International Symposium on Antennas and Propagation and CNC/USNC/URSI Radio Science Meeting*, 1, 2010.

9. Shea, J. D., P. Kosmas, B. D. Van Veen, and S. C. Hagness, "Three-dimensional microwave imaging of realistic numerical breast phantoms via a multiple-frequency inverse scattering technique," *Medical Physics*, Vol. 37, 4210–4226, Aug. 2010.
10. Johnson, J. E., et al., "Advances in 3D forward-backward time-stepping (FBTS) inverse scattering technique for breast cancer detection," *IEEE Trans. Biomed. Eng.*, Vol. 56, 2232–2243, Sept. 2009.
11. Fhager, A., et al., "Reconstruction quality and spectral content of an electromagnetic time-domain inversion algorithm," *IEEE Trans. Biomed. Eng.*, Vol. 53, 1594–1604, Aug. 2006.
12. Benedetti, M., et al., "Multiple-shape reconstruction by means of multiregion level sets," *IEEE Trans. Geosc. and Remote Sensing*, Vol. 48, 2330–2342, May 2010.
13. Benedetti, M., et al., "A multi-resolution technique based on shape optimization for the reconstruction of homogeneous dielectric objects," *Inverse Problems*, Vol. 25, 1–26, 2009.
14. Benedetti, M., et al., "A two-step inverse scattering procedure for the qualitative imaging of homogeneous cracks in known host media-Preliminary results," *IEEE Ant. and Wireless Prop. Letters*, Vol. 6, 592–595, 2007.
15. Eskandari, M. and R. Safian, "Inverse scattering method based on contour deformations using a fast marching method," *Inverse Problems*, Vol. 26, 1–19, 2010.
16. Woten, D. A., et al., "Experimental microwave validation of level set reconstruction algorithm," *IEEE Trans. Antennas and Propag.*, Vol. 58, 230–233, Jan. 2010.
17. Irishina, N., M. Moscoso, and O. Dorn, "Microwave imagining for early breast cancer detection using a shaped-based strategy," *IEEE Trans. Biomed. Eng.*, Vol. 56, 1143–1153, Apr. 2009.
18. Kurrant, D. J. and E. C. Fear, "Technique to decompose near-field reflection data generated from an object consisting of thin dielectric layers," *IEEE Trans. Antennas and Propag.*, 2011 (submitted).
19. Spagnolini, U., "Permittivity measurements of multilayered media with monostatic pulse radar," *IEEE Trans. Geosci. Remote Sens.*, Vol. 35, 454–463, Mar. 1997.
20. Spagnolini, U. and V. Rampa, "Multitarget detection/tracking for monostatic ground penetrating radar: Application to pavement profiling," *IEEE Trans. Geosci. Remote Sens.*, Vol. 37, 383–394, Jan. 1999.

21. Sill, J. M. and E. C. Fear, "Tissue sensing adaptive radar for breast cancer detection and experimental investigation of simple tumor models," *IEEE Trans. Microwave Theory Tech.*, Vol. 53, 3312–3319, Nov. 2005.
22. Bourqui, J., M. Okoniewski, and E. Fear, "Measurement of microwave frequency signals transmitted through the human breast," *Proc. AP-S/URSI*, 1, Spokane, Wash, USA, 2011.
23. Sill, J., et al., "Realistic breast models for second generation tissue sensing adaptive radar system," *Proc. EuCAP*, 1–4, Nov. 2007.
24. Pope, T. L., et al., "Breast skin thickness:Normal range and causes of thickening shown on film-screen mammography," *J. Can. Assoc. Radiologists*, Vol. 35, 365–368, 1984.
25. Kurrant, D. J. and E. C. Fear, "Regional estimation of the dielectric properties of the breast: skin, adipose, and fibroglandular tissues," *Proc. EuCAP*, 2920–2924, Rome, Italy, 2011.
26. Belkebir, K., et al., "Validation of 2D inverse scattering algorithms from multi-frequency experimental data," *Journal of Electromagnetic Waves and Applications*, Vol. 14, No. 12, 1637–1667, 2000.
27. Geffrin, J., P. Sabouroux, and C. Eyraud, "Free space experimental scattering database continuation: Experimental setup and measurement precision," *Inverse Problems*, Vol. 21, S117–S130, Dec. 2005.
28. Bourqui, J., E. Fear, and M. Okoniewski, "Versatile ultrawide-band sensor for near-field microwave imaging," *Proc. EuCAP*, 1–5, Barcelona, Spain, Apr. 12–16, 2010.